An Online Gas Chromatography Cell Setup for Accurate CO2-Electroreduction Product Quantification

Journal of The Electrochemical Society

An Online Gas Chromatography Cell Setup for Accurate CO_2-Electroreduction Product Quantification

Journal of The Electrochemical Society, 2021 **168** 064504

An Online Gas Chromatography Cell Setup for Accurate CO_2-Electroreduction Product Quantification

Justus S. Diercks,[1,*] Bernhard Pribyl-Kranewitter,[1] Juan Herranz,[1,,z] Piyush Chauhan,[1] Antoine Faisnel,[1] and Thomas J. Schmidt[1,2,***]**

[1]*Electrochemistry Laboratory, Paul Scherrer Institut—5232 Villigen PSI, Switzerland*
[2]*Laboratory of Physical Chemistry, ETH Zurich—8093 Zurich, Switzerland*

The electrochemical reduction of carbon dioxide (CO_2) constitutes an increasingly important scientific topic and research on novel electrocatalysts for this demanding reaction is constantly increasing. One of the most important properties to be inferred for such electrocatalysts is their product selectivity and potential dependence thereof. However, the wide range of materials currently employed in CO_2 electroreduction (e.g., Ag, Cu, Pd) entails a large variety of gaseous and/or liquid reaction products for which accurate quantification implies a major challenge. With this motivation, in this study we present an online gas chromatography cell setup specifically designed for the accurate and reproducible determination of the product selectivities of CO_2-reduction electrocatalysts. Therewith, we assess the parameters influencing the cell's performance and point out important design features, such as reproducible electrode alignment, minimized contact resistances and a low ratio among electrolyte volume and the electrodes' geometrical surface area. The setup was validated by performing measurements on a Pt nanoparticle catalyst for which H_2 is the only expected reduction product, while a Pd nanoparticle catalyst was subsequently used to verify its capabilities for CO_2 electroreduction selectivity measurements involving multiple liquid and gaseous products.
 [DOI: 10.1149/1945-7111/ac0363]

Manuscript submitted March 8, 2021; revised manuscript received May 11, 2021. Published June 8, 2021.

Supplementary material for this article is available online

The electrochemical reduction of carbon dioxide (or CO_2-reduction reaction, CO_2RR) to value-added products (e.g., CO, formate)[1,2] is expected to play a key role in a future carbon-neutral society. Due to the kinetic sluggishness and mixed product selectivity associated with this reaction, many efforts continue to be devoted to the development of improved CO_2RR-electrocatalysts. Currently, these include Cu-, Sn-, Au-, Ag- or Pd-based materials (and combinations thereof), which are often processed in the form of nanoparticles that can additionally be featured as alloys,[3–5] core-shell structures,[6–8] and/or display controlled shapes.[9–12] While for other electrocatalytic processes implying the evolution of a gas (e.g., H_2, O_2) only one product is obtained and the measured electrochemical current can be directly regarded as indicative of a product-specific catalytic activity, the simultaneous production of several CO_2-reduction products (and the competing H_2-evolution reaction, HER) makes this principle inapplicable to the CO_2RR. Consequently, electrocatalytic studies for this reaction systematically imply the determination of a given material's potential dependent selectivity towards the variety of CO_2RR-products (including side-evolved H_2) that can be obtained. These species can largely differ among catalysts, and thus while Au and Ag mostly yield gaseous products (i.e. CO and H_2), for Sn (H_2, formate), Pd (H_2, CO, formate) and Cu (H_2, CH_4, C_2H_4, alcohols) both gases, liquids and/or ionic species are produced in significant amounts.[13] As a result, the accurate quantification of the fraction of the overall current devoted to the production of the specific products (or Faradaic efficiency, FE) often relies on the combination of several analytic techniques. More precisely, gaseous products are mostly analyzed by online electrochemical mass spectrometry (OLEMS),[14–17] or online gas chromatography (online GC),[18–21] while liquid species can be quantified using high-performance liquid chromatography (HPLC),[19,22] nuclear magnetic resonance spectroscopy (NMR),[18,21,23–26] or (for ionic species like formate) ion-exchange chromatography (IC).[20,27] Thus, two or more analysis methods (i.e., for gaseous, liquid and sometimes ionic species) often need to be combined to enable accurate and complete quantification of all CO_2RR-products. This leads to often underestimated challenges in the accurate detection of all CO_2RR-products and the subsequent assignment of their contributions to the overall measured current, which should consequently result in a total FE of ≈100%.

While (micro)fluidic reactors[28,29] and co-electrolyzer cells[17,30] implementing gaseous reactants in combination with gas diffusion electrodes and polymer electrolytes are becoming increasingly popular in the field of CO_2RR, the complex interplay of the variables that define these devices' performance renders them ill-suited for evaluating CO_2-electroreduction catalysts. Instead, the most often used setups for such catalyst evaluation are "H-type" glass cells consisting of two electrolyte-filled chambers containing vertically-immersed working- and counter-electrodes, separated by an ion-exchange membrane that minimizes crossover of CO_2RR-products and their subsequent oxidation on the anode. More recently, Moreno-García et al.[31] have presented a novel CO_2-electroreduction setup consisting of an inverted rotating disk electrode (RDE) allowing controlled mass flow and combined with GC product detection. Beyond this novelty, this and the above setups feature a relatively large ratio between electrolyte volume and working electrode surface that leads to low concentrations of liquid products, rendering their subsequent quantification difficult.

The above-described issues were successfully addressed by Kuhl et al.[18] using a parallel plate cell with online GC and post-electrochemistry analysis of liquid products through ^{1}H-NMR. A resembling parallel plate cell heavily inspired in that design was successfully used by our group,[32,33] and we have iteratively refined its design to improve the reproducibility of the electrodes' alignment, minimize ohmic contact losses and facilitate its assembly. In doing so, we also found eventual pitfalls faced in the measurements conducted with these types of cells and the subsequent product quantification and selectivity determination which, to the best of our knowledge, have so far not been discussed in the literature.

Therefore, in this work, we present an online gas chromatography cell setup based on a parallel plate design allowing reproducible assembly and electrode alignment while featuring a low contact resistance, minimized headspace and low electrolyte-to-electrode-surface ratio. Additionally, we provide guidelines to conduct such CO_2-electroreduction measurements in a successful and reproducible manner.

*Electrochemical Society Student Member.
**Electrochemical Society Member.
***Electrochemical Society Fellow.
[z]E-mail: juan.herranz@psi.ch

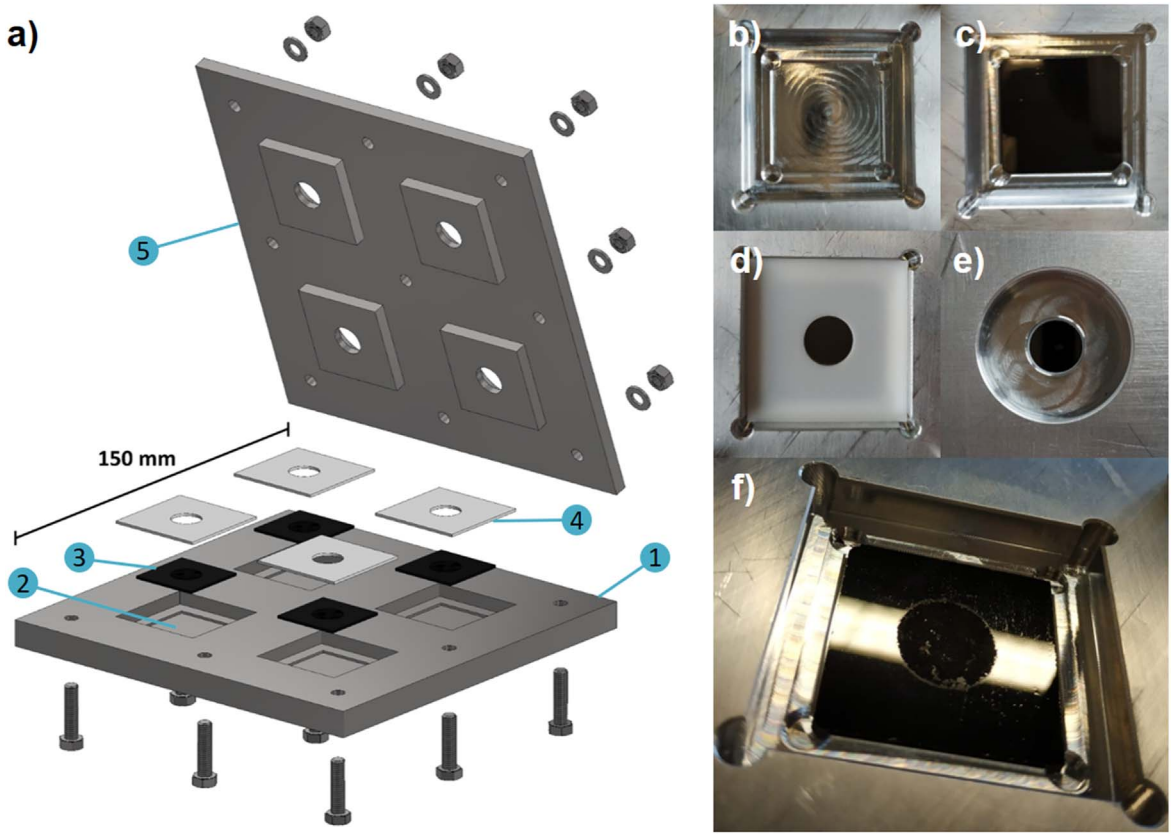

Figure 1. Technical drawing of the drop-casting setup (a), consisting of an aluminum base plate (a–1), featuring 4 square slots (a–2 and b) on which the 2.5 × 2.5 cm^2 glassy carbon plates (a-3 and c) are positioned. These are each covered by a 1 mm thick piece of PTFE with a 1.1 cm diameter hole at its center (a-4 and d) and a top cover with holes matching those of the PTFE masks (a-5 and e) that is closed using the nine lateral screws. An example of an electrode of 20% Pd/C with a loading of 100 $\mu g_{Pd} \cdot cm^{-2}$ prepared with this setup is shown in (f).

Experimental

Electrode preparation.—For the validation of the cell, two commercial carbon-supported Pd and Pt nanoparticle catalysts were used, namely 20% Pd on Vulcan XC-72 (Premetek P30A200, Lot No. 100237) and 47% Pt on Ketjenblack EC600JD (Tanaka Kikinzoku Kogyo K.K., TEC10E50E). Inks of these catalysts were prepared by dispersing a weighed amount of powder (≈50 mg) in ultrapure water (18.2 MΩ·cm, ELGA Purelab Ultra) and isopropanol (Sigma-Aldrich, HPLC grade, 99.9%), using an H_2O-to-isopropanol volume ratio of 70:30. Thereafter, an aliquot of Nafion perfluorinated resin solution (Sigma-Aldrich, 5%) was added in the amount required to yield a Nafion-to-carbon mass ratio of 0.2. The resulting ink was ultrasonicated (VWR USC100T) for 15 min, again ultrasonicated for 30 s in between the preparation of electrode sets and discarded after the preparation of three sets of four electrodes.

Glassy carbon plates (Goodfellow Cambridge, 3000 C, cut to 2.5 × 2.5 cm^2) were used as a substrate for these nanoparticle catalysts and were machine mirror-polished using aluminum oxide powders of 0.3 and 0.05 μm grain size (PRÜFAG, MicroPolish) prior to this use. Drop-casting of the so-prepared inks was chosen as the electrode preparation technique to ensure a controllable loading of the catalysts. The solvent volumes, as well as the ionomer dispersion in the inks, were adjusted so that an ink drop of 25 μl pipetted on the 0.96 cm^2 electrodes (vide infra) yielded a precious metal loading of 100 or 25 $\mu g_{metal} \cdot cm^{-2}$ for Pd/C vs. Pt/C, respectively. This pipetted drop was confined to the desired, round electrode geometry (1.1 cm in diameter, 0.96 cm^2 in area) using the drop-casting setup schematized in Fig. 1a. The latter consisted of an aluminum base plate featuring four slots (Fig. 1b) that accommodated the same number of mirror-polished glassy carbon plates (Fig. 1c) that were individually covered by 1 mm thick, framing pieces of polytetrafluoroethylene (PTFE) foil, with a 1.1 cm diameter hole at their center (Fig. 1d). This assembly was then covered again by a top plate featuring four 1.1 cm diameter holes with their center matching those of the four glassy carbon plates. Nine lateral screws were inserted and tightened to a torque of 5 N·m to compress the PTFE framing foils and seal the setup (Fig. 1e). Thereafter, the assembly was placed in a desiccator (Faust AG, PC/PP 250 mm) and the ink drops (25 μl) were pipetted onto the exposed areas of the PTFE-sealed glassy carbon plates. Then, the desiccator was closed, evacuated to 20 mbar (KNF LABOPORT N 842.3 FT.18) and held at this pressure for one minute. Thereafter, the desiccator was vented, the electrode preparation assembly was taken out of it and disassembled, yielding four glassy carbon plates with circular catalyst layers of 0.96 cm^2 and loadings of 100 $\mu g_{Pd} \cdot cm^{-2}$ or 25 $\mu g_{Pt} \cdot cm^{-2}$ at their center (cf. Fig. 1f).

Cell design.—The newly developed cell (Fig. 2) consists of four main parts, hereafter referred to as working electrode current collector (2), working electrode compartment (11), counter electrode compartment (15), and counter electrode current collector (18). The material chosen for the current collectors was stainless steel (WNr. 1.4404), while the electrode compartments were made out of polyether ether ketone (PEEK), inert towards both mildly acidic and alkaline electrolytes while easily machineable and providing sufficient mechanical stability to compress the PTFE gaskets.

To assemble the cell, four hexagon head, 60 mm long M5 screws (1) were inserted from the bottom into the respective holes of the working electrode current collector, which was subsequently laid on the lab bench with the screws facing upwards. Thereafter, a 2.5 × 2.5 cm^2 piece of graphite foil (Graphit Kropfmühl GmbH, 0.4 mm

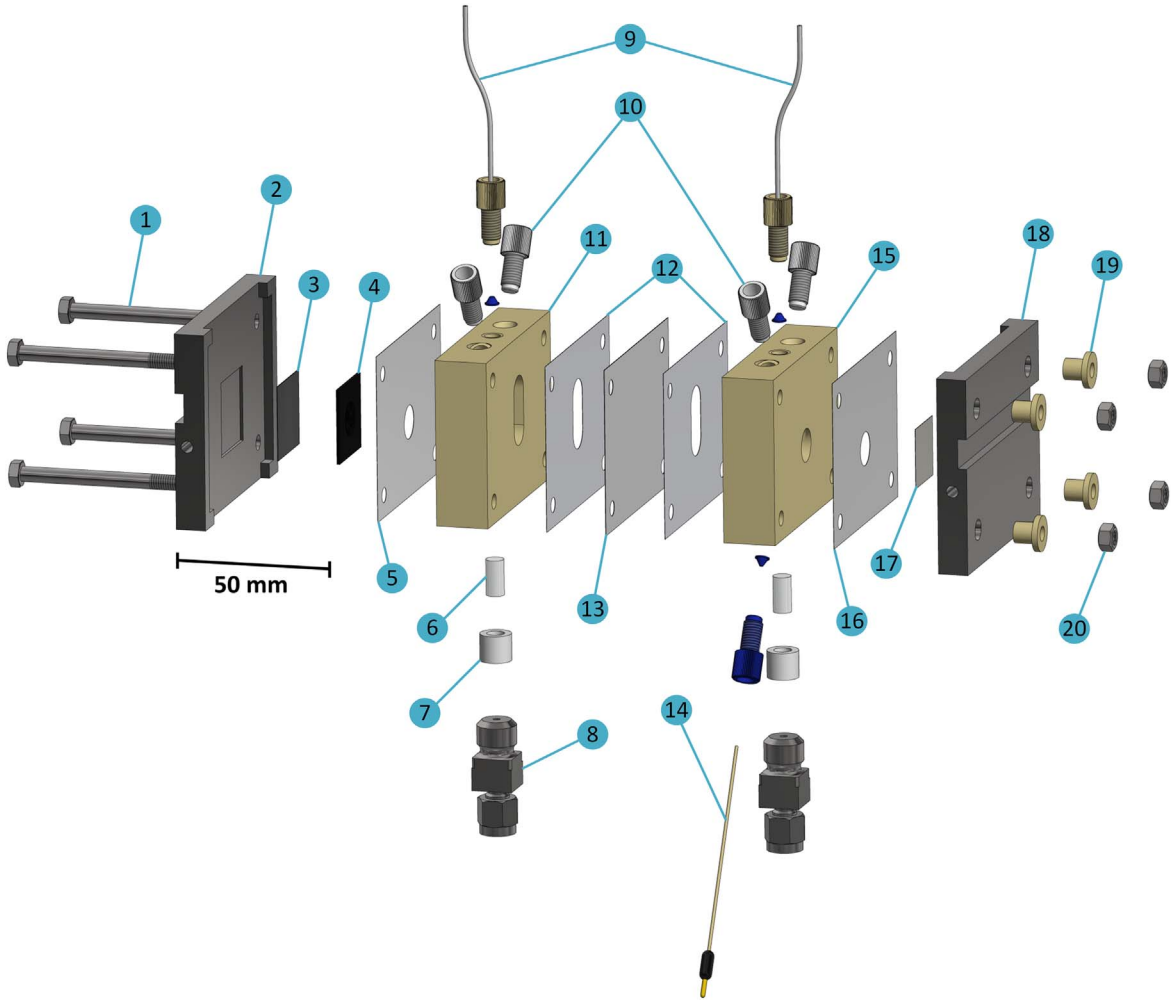

Figure 2. Technical drawing of the cell assembly, consisting of four M5 screws (1), the cathode current collector (2), a piece of graphite foil (3), the glassy carbon plate with the drop-casted working electrode (4), PTFE gaskets (5, 12, 16), porous glass frits (6), PTFE frit holders (7), input line adapter screws (8), product output lines (9), PTFE plugs (10), the working electrode compartment (11), a piece of Nafion XL membrane (13), a leak-free Ag/AgCl reference electrode (14), the counter electrode compartment (15), the platinum counter electrode (17), the counter electrode current collector (18), and the PEEK inserts (19) and nuts (20) to close the assembly.

thickness—3) was placed at the center of the current collector's central slot (1 mm in depth), and the previously prepared glassy carbon plate (4) with the drop-casted catalyst facing upwards was placed on top of it. The gas bubblers were inserted into both electrode compartments before assembly by placing the glass frits (ROBU, 6 mm diameter, #2 porosity—6) inside their cylindrical PTFE holders (7), placing these assemblies in the electrode compartments and compressing the holders around the frits by inserting and tightening the gas line adapter screws (Swagelog, SS-3M0-1-4RP—8). Additionally, the leak-free reference electrode (Ag/AgCl, Harvard Apparatus, LF-1—14) was screwed into the counter electrode compartment, since positioning it in the working electrode reservoir could influence the CO_2RR product selectivity due to the leakage and plating of Ag^+.[34]

Next, the working electrode was covered with a 100 μm thick piece of PTFE foil with fitting cutouts for the screws and the electrode catalyst layer (0.96 cm^2 in area—5). Thereafter, the working electrode compartment (11) was placed atop the PTFE foil, followed by a second PTFE foil piece (12) and the membrane (Chemours, Nafion XL—13). This was followed by another PTFE foil piece (12), the counter electrode compartment (15) and a fourth PTFE gasket (16). The cell assembly was finalized by placing a 2.5 × 2.5 cm^2 piece of 0.05 mm thick Pt-foil (Alfa Aesar, 99.99%—17) as the counter electrode, and the assembly was closed using the counter electrode current collector piece (18). Finally, four PEEK sleeves (19) were inserted into the counter electrode current collector to avoid short-circuiting the two electrodes, and the cell was compressed by putting four nuts (20) over the screws and tightening them to a torque of 2 N·m.

Using the above-described assembly, the contact resistance between the catalyst drop-casted on the glassy carbon or the platinum foil used as working- vs. counter-electrodes and their corresponding, stainless steel current collectors accounted for ≈0.6 Ω.

Measurement procedure.—The electrode compartments, PTFE screws, and gaskets were cleaned by boiling in a 3:1 mixture of ammonia solution (NH_4OH, 25%, Merck EMSURE) and hydrogen peroxide (H_2O_2, 30%, Merck EMSURE), followed by rinsing them a minimum of three times with ultrapure water before additionally boiling them three times in ultrapure water. The 0.5 M bicarbonate electrolyte was prepared by mixing 12.515 g of potassium bicarbonate ($KHCO_3$, Honeywell, 99.95% trace metals basis) in 250 ml of ultrapure water. The measured pH (Metrohm 913 pH meter with Metrohm Unitrode 6.0258.010) of this electrolyte was 7.3 when saturated with CO_2 (Messer AG, 5.5 quality). The 0.5 M potassium phosphate buffer (K_2HPO_4/KH_2PO_4-buffer) was set to be close to neutral pH at a value of 6.8 when saturated with N_2 or H_2, by mixing 1.816 g of di-potassium hydrogen phosphate (K_2HPO_4, Merck LiChropur, anhydrous, 99.999%) and 1.984 g potassium dihydrogen

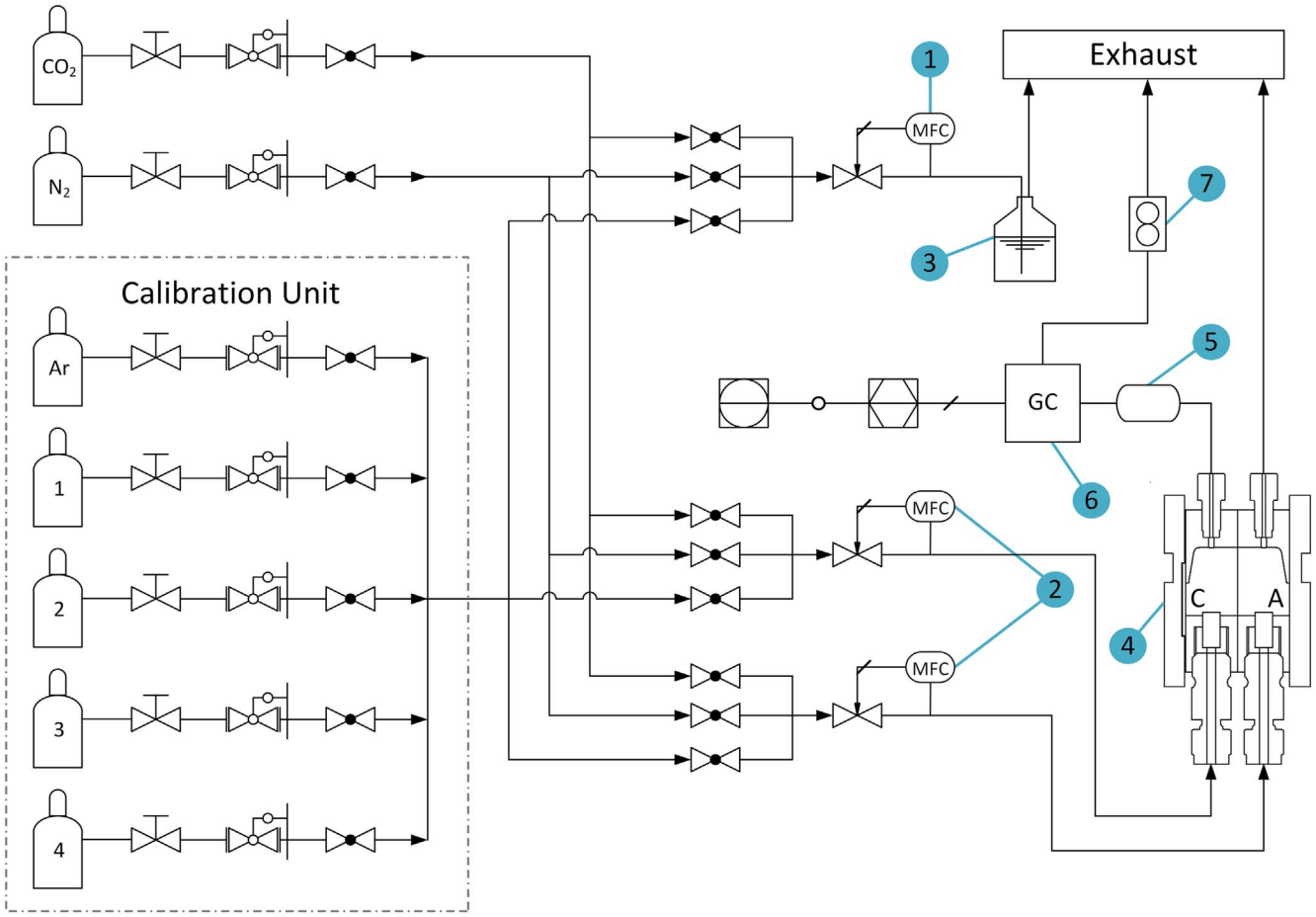

Figure 3. Piping and instrumentation diagram (PID) of the online gas chromatography (GC) cell setup including mass flow controllers (MFCs) for electrolyte pre-saturation (1), cell inlet gas flows (2), the electrolyte reservoir (3), the electrochemical parallel plate cell (4), a product gas homogenization reservoir at the catholyte outlet (5), followed by the GC (6) and a downstream mass flow meter (7). Note that in the parallel plate cell (4) the reservoirs labeled as "C" and "A" refer to the catholyte and anolyte (or working- vs. counter-electrode) compartments, respectively.

phosphate (KH_2PO_4, Merck, LiChropur, anhydrous, 99.999%) in 50 ml of ultrapure water. The membrane (Chemours, Nafion XL) was soaked overnight in the respective electrolyte of choice prior to its use. The Ag/AgCl reference electrode was pre-calibrated against the reversible hydrogen electrode (RHE) scale by performing an H_2-oxidation/evolution measurement on a polycrystalline platinum rotating disk electrode (RDE) in H_2-saturated 0.5 M K_2HPO_4/KH_2PO_4-buffer. The corresponding calibration potential for the measurements in CO_2-saturated 0.5 M $KHCO_3$ electrolyte was estimated by subtracting 29.5 mV from the potential determined in the H_2-saturated K_2HPO_4/KH_2PO_4 buffer.

To start each electrochemical measurement, the cell was assembled according to the above-described procedure and the gas inlets were connected to two mass flow controllers (Bronkhorst, IN-FLOW F201-CI) flowing N_2 (Carbagas AG, 6.0) or CO_2 (Messer AG, 5.5) at a flow rate of 10 ml min^{-1} for both compartments, as to avoid a pH gradient between them. The cell compartments' outlets were furthermore connected to the downstream gas lines using the respective screws (IDEX P-255 with P-359), connecting the working electrode outlet to a homogenization volume (Swagelok, SS-4CD-TW-50) followed by the injection loop of the GC. Both electrode compartments were subsequently filled with 3 ml of N_2- or CO_2-presaturated electrolyte. Thereafter, the cell compartments' holes used for electrolyte dosing were closed with four PTFE screws (IDEX P-316) and the current collectors, as well as the reference electrode, were connected to the potentiostat (BioLogic, VSP-300). An image of the cell assembly during operation can be found in Fig. S1 (available online at stacks.iop.org/JES/168/064504/mmedia).

After further gas saturation of both electrolyte compartments for five minutes, electrochemical impedance spectroscopy was recorded in between 1 MHz and 1 Hz, applying a 10 mV perturbation at the open-circuit voltage (OCV) to obtain a Nyquist plot (see an example in Fig. S2) from which the corresponding high-frequency resistance (HFR) was derived. This HFR was subsequently used to digitally iR-compensate 85% of the potential applied in the subsequent electrochemical measurements. Note that the remaining 15% of the resistive losses were manually corrected in the subsequent processing of the results. Thereafter, the electrodes were electrochemically conditioned by recording 20 cyclic voltammograms (CVs) at 100 mV s^{-1}, ten CVs at 50 mV s^{-1}, and two CVs at 10 mV s^{-1} between 0.05 and 1.2 V vs. the reversible hydrogen electrode (V_{RHE}). After conditioning, a one-hour chronoamperometry experiment was run at a fixed potential, while GC spectra were acquired. Once this potential hold was completed, the cell's four top screws were removed and, for the measurements employing Pd/C, the electrolyte in the working electrode compartment (so-called "catholyte") was extracted using a syringe and transferred into a vial for later IC analysis. The counter electrode compartment electrolyte ("anolyte") was also extracted but discarded, since previous IC measurements found negligible concentrations of formate in this compartment, due to very low crossover and/or electrooxidation of any produced species. Thereafter the cell was partly disassembled to exchange the working electrode with a new one. After this reassembly, the inner cell compartments were rinsed twice by fully filling them with electrolyte and disposing of it, and were subsequently refilled with 3 ml of electrolyte. Thereafter, the measurement

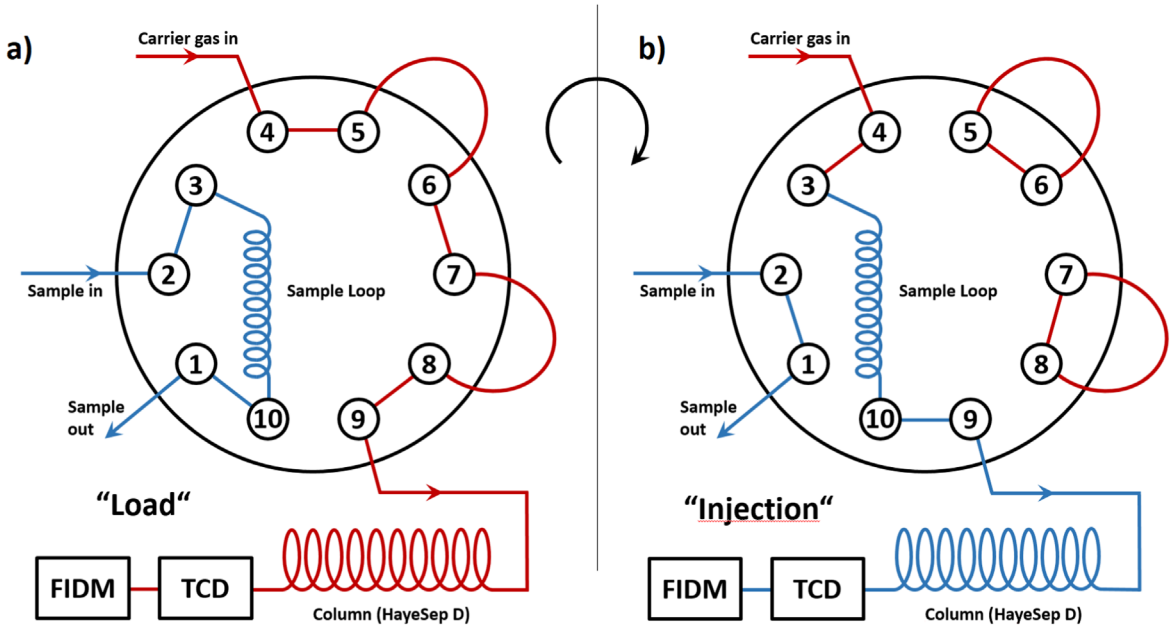

Figure 4. Schematic of the 10-way valve switching mechanism of the gas chromatograph. In the "load" mode (a), the product gas is continuously flushed through a sample loop while the carrier gas flows to the column and detectors. Upon sample injection (b), the switching of the valves' mode isolates the filled sample loop from the product stream, and this filled volume is flushed to the column and detectors by the carrier gas (here, Ar).

was restarted for the next potential applying the above-described conditioning procedure and subsequent potential hold. All CO_2 electroreduction experiments were performed three times and the average product distribution values at each potential are reported in what follows.

CO_2RR product analysis.—The detection of the products was done separately for gases and dissolved ionic species (i.e. formate). For the detection of formate, an ion chromatograph (Metrohm, 882 Compact IC plus) coupled with an autosampler (Metrohm, 863 Compact) and an anion exchange column (Metrosep, A Supp 5—150/4.0) was used. The eluent was prepared by mixing 0.168 mg of sodium bicarbonate ($NaHCO_3$, Sigma-Aldrich, 99.7%) with 0.678 mg of sodium carbonate (Na_2CO_3, Sigma-Aldrich, 99.5%) in 2 l of ultrapure water, while 0.1 M H_2SO_4 was used for suppressor regeneration. The IC was calibrated using seven standards created on the base of a commercial 1000 ppm solution (VWR, formate 1000 mg·l^{-1}, 100 ml). The calibration values can be found in Table S1, while the calibration curve is displayed in Fig. S3. Three injections of 20 μl were carried out for each sample, whereby the necessary flushing of the system required a total volume of 10 ml per sample. Therefore, 0.5 ml of extracted catholyte was diluted with 9.5 ml of ultrapure water to yield 10 ml of a 1:19 diluted sample. The formate concentrations derived from the three injections were later averaged and multiplied by 20 to give the concentration of formate in the electrolyte.

As for the gaseous CO_2RR-products, their concentration was quantified in a gas chromatograph (GC - SRI Instruments, 8610 C), with software (PeakSimple 4.88) enabling automated gas injections using an autosampler function. To ensure a consistent result from the GC, the product gas stream from the cell was first fed through a metal chamber (Swagelok, SS-4CD-TW-50, Fig. S1) to homogenize the gas mixture before it was led through the sample loop of the GC. After exiting the latter, the product gas stream was passed through a mass flow meter calibrated for CO_2 (Bronkhorst, IQ$^+$Flow 100 C MFM), enabling the comparison of inlet and outlet gas flows[35] that allows the verification of the tightness of the cell and tubing. The outlet gas streams of both electrodes were finally bubbled through water-filled vials to assure similar backpressures on both sides and to visibly track inconsistencies in the gas flows. A schematic

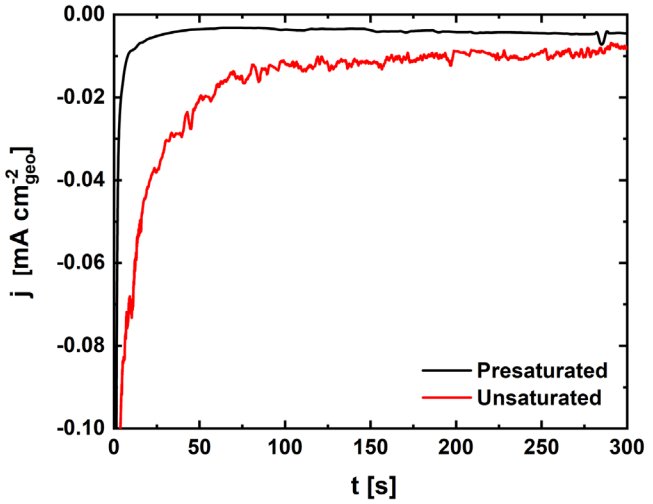

Figure 5. Time evolution of the initial current densities during a potentiostatic hold at 0.4 V_{RHE} recorded immediately after filling the cell compartments with N_2-pre-saturated or unsaturated 0.5 M K_2HPO_4/KH_2PO_4-buffer. Note that catholyte and anolyte were constantly purged with N_2 at a flow rate of 10 ml·min^{-1} directly after cell assembly and that the working electrode was Pt/C with a loading of 25 μg_{Pt}·cm^{-2}.

representation of the components and general setup is shown in Fig. 3 in the form of a piping and instrumentation diagram (PID).

The gas chromatograph was used in a 10-way valve configuration illustrated in Fig. 4. In its "load" mode (cf. Fig. 4a), the CO_2RR-product stream leaving the catholyte's outlet is not sampled for analysis and instead is bypassed through the valve's 1 ml sample loop to the exhaust line, while the chromatography column and detectors are constantly flushed with the carrier gas (Ar—Carbagas AG, 6.0–2 bar column pressure). Complementarily, in the "injection" mode (cf. Fig. 4b), the sample loop filled with product gas in the previous "load" step is flushed to the column (9' Hayesep D) by the argon carrier stream. The separated gas mixture is then circulated through a non-destructive thermal conductivity detector (TCD) for hydrogen detection with a lower quantification limit for H_2 of

≈10 ppm. Thereafter, the gas is fed to a methanizer that converts all carbon species to methane (CH_4) using an H_2 stream, which is subsequently combusted in a flame-ionization detector (FID) with a lower quantification limit of ≈1 ppm for carbon monoxide (CO). Notably, the exclusive gas product selectivity towards H_2 and (in the case of Pd/C) CO production displayed by the Pt- and Pd-based catalysts included in this study enabled us to operate the column at a constant temperature of 70 °C with injections carried out every five minutes. The analysis of hydrocarbons (e.g., C_2H_4 or C_2H_6) with longer retention times at this temperature and the potential requirement of higher column oven temperatures including temperature ramps (for peak separation) and subsequent cooldown times for the analysis of these products can result in a much lower injection frequency.[32] While this detection method was not used in this work, liquid injections into the GC additionally enable the quantification of lower alcohols (e.g., methanol, ethanol) with an additional column (6′ × 1/8′ S.S. Hayesep D) and an additional FID.

The calibration of the GC was carried out by flowing four calibration gas mixtures through the cell, with CO- and H_2-concentrations ranging between 50 and 1000 as well as 100 and 10000 ppm, respectively (see Table SI for the precise compositions, and the corresponding calibration lines in Fig. S3). As the GC setup was previously used for investigations of the selectivity of copper catalysts,[32] methane and ethylene were also included in the calibration gas mixtures. A typical chromatogram of both the FIDM and TCD detectors for a calibration mixture including H_2, CO, ethylene and methane can be found in Fig. S4.

RDE measurements.—Thin-film rotating disk electrode (RDE) voltammetry[36] was used for validating the utilization of the catalysts in the novel cell design. The RDEs were prepared by drop-casting onto a mirror-polished, 5 mm diameter glassy carbon disk (HTW Hochtemperatur-Werkstoffe) an ink of catalyst prepared using the same procedures specified above for the preparation of electrodes for the online GC cell, with the solvents being adjusted to yield precious metal loadings of 25 and 100 $\mu g_{metal} \cdot cm^{2}$ for Pt/C and Pd/C, respectively, using an 8 μl drop. The disk was embedded in a PTFE RDE tip (Pine Research), which was connected to a rotation controller (Pine Research) and used as a working electrode in a custom-built glass cell (Schmizo AG). A gold mesh (Advent Research Materials) and an Ag/AgCl electrode (Harvard Apparatus, LF-1) pre-calibrated vs. the RHE scale in the same electrolyte were inserted in individual glass compartments separated by glass frits (Ametek G0300, 4 mm diameter) and used as counter and reference electrodes, respectively. Since the measurements were used as a comparison to those performed in the online GC cell, all other parts of the setup (gases, potentiostat, electrolyte, conditioning, etc.) were kept unchanged among measurement environments.

To infer a possible effect of the high catalyst loading of the Pd/C catalyst used in the online GC cell on its electrochemical surface area, CO-stripping measurements were carried out in this RDE configuration. To this end, an RDE prepared as described above was electrochemically conditioned by recording a minimum of ten CVs at 100 mV s^{-1}, followed by five CVs at 50 mV s^{-1}, two CVs at 50 mV s^{-1}, and two CVs at 10 mV s^{-1} between 0.05 and 1.2 V_{RHE}. Subsequently, a potential hold at 0.4 V_{RHE} was carried out for 30 min, while the previously N_2-saturated solution was purged with CO for five minutes followed by N_2 purging for 25 min. The CO-stripping sweep was run at 10 mV s^{-1} from the holding potential to the negative inversion potential of 0.05 V_{RHE}, thereafter positively to 1.25 V_{RHE} and followed by several cycles in this potential window. The specific charge used to calculate the ECSA from the CO-stripping charge was 2·205 $\mu C \cdot cm_{Pd}^{-2}$.[37]

Results and Discussion

Electrolyte presaturation, catalyst layer utilization and cell convection properties.—We start our investigation by assessing some of the online GC cell's properties determining its electrochemical performance. In this regard, and as stated above, the electrolyte was presaturated with the gas of choice (N_2 or CO_2) by bubbling the latter through a bottle filled with this solution for ≈20 min prior to the dosing of the electrolyte inside the cell's anolyte and catholyte. The importance of this pre-saturation step is illustrated in Fig. 5, displaying the current response over five minutes of a potential hold at 0.4 V_{RHE} immediately after assembly of the cell filled with non-pre-saturated vs. N_2 pre-saturated electrolyte (0.5 M K_2HPO_4/KH_2PO_4-buffer) using a Pt/C working electrode. Notably, the unsaturated electrolyte features a significant reduction current over the first 100 s of the potentiostatic hold and fails to reach the saturation level of the pre-saturated electrolyte (displaying a residual current < 10 $\mu A \cdot cm^{-2}$). Under such potentiostatic conditions and potential of choice, this measured current on such a Pt/C electrode (beyond the initial transient) can be ascribed to the reduction of residual O_2 dissolved in the electrolyte, which should lead to products (H_2O and/or H_2O_2) that are not detected by a CO_2RR setup. This shall in terms lead to an underestimation of the corresponding Faradaic efficiency values that may be negligible over long potential holds at large currents and corresponding overpotentials, but which becomes a significant source of error in short potentiostatic holds at low current densities and overpotentials.

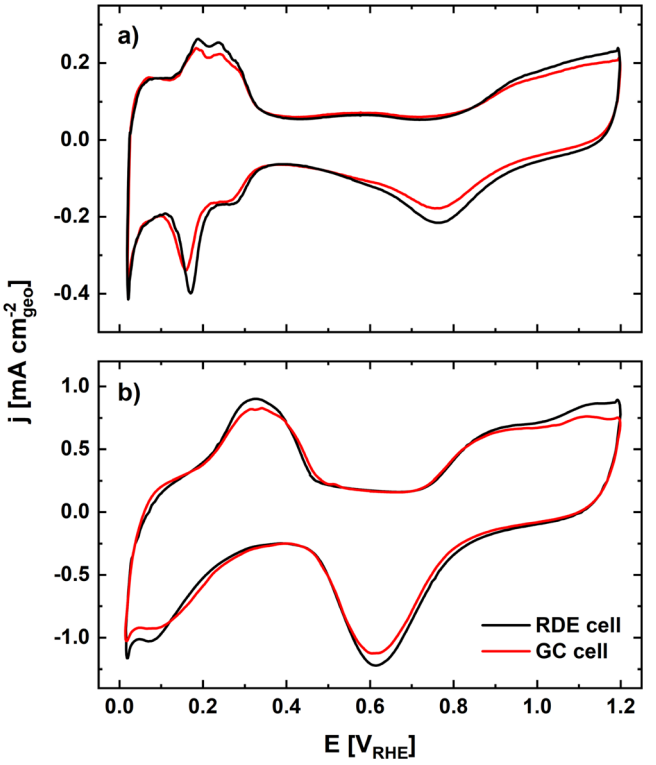

Figure 6. Comparison of the cyclic voltammograms (at 10 mV s^{-1}) recorded in rotating disk electrode (RDE) configuration vs. the online gas chromatography (GC) cell in N_2-saturated, 0.5 M K_2HPO_4/KH_2PO_4-buffer on a 47% Pt/C electrode with a loading of 25 $\mu g_{Pt} \cdot cm^{-2}$ (a) and in CO_2-saturated 0.5 M $KHCO_3$ on a 20% Pd/C electrode with a loading of 100 $\mu g_{Pd} \cdot cm^{-2}$ (b).

Another crucial feature of every electrochemical setup is that it should reliably assure an as-high-as-possible utilization of the working electrode catalyst layer (CL). This is especially important in cells that are designed for product quantification or spectroscopic purposes, since these often imply the implementation of highly loaded catalyst layers (as to attain a better spectroscopic signal or to increase the amount of product per electrolyte volume) with concomitantly large thicknesses that may only be partially wetted with electrolyte.[38,39] This potential issue is well illustrated by the Pt/C and Pd/C catalyst layers used throughout this study. Specifically, considering the metal loadings of 25 $\mu g_{Pt} \cdot cm^{-2}$ vs. 100 $\mu g_{Pd} \cdot cm^{-2}$ used in their electrodes, along with the catalysts'

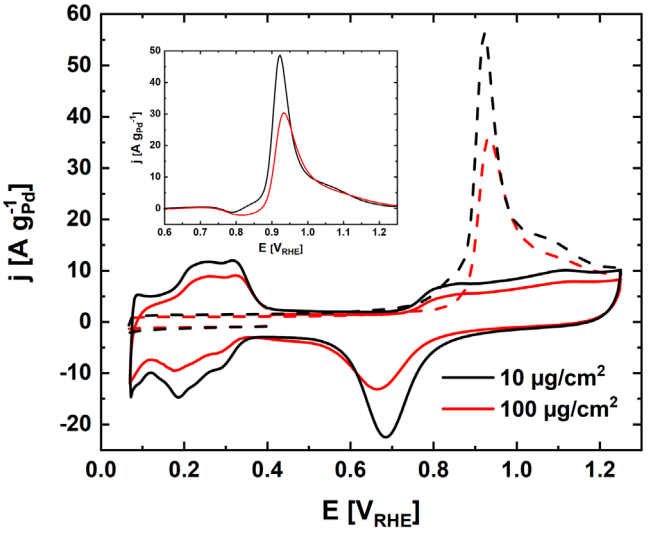

Figure 7. Comparison of CO-stripping sweeps (dashed lines) and baseline cyclic voltammograms (solid) at 10 mV·s^{-1} recorded in rotating disk electrode (RDE) configuration in N_2-saturated, 0.5 M K_2HPO_4/KH_2PO_4-buffer on a 20% Pd/C electrode with loadings of 10 vs. 100 $\mu g_{Pd} \cdot cm^{-2}$. The inset shows the baseline-subtracted CO-stripping currents densities.

carbon weight fractions (53 vs. 80% for Pt/C vs. Pd/C) and the ionomer-to-carbon mass ratio of 0.2 used in the inks' formulation (*vide supra*), and assuming density values of ≈2 g·cm^{-3} for carbon and ionomer along with a film porosity of ≈ 50%, the estimated CL thicknesses account to ≈0.3 vs. ≈4.8 μm for Pt/C vs. Pd/C, respectively. Thus, while the former is well below the ≈1 μm threshold for which complete catalyst layer utilization can be expected, the greater thickness of the Pd/C catalyst layer calls for verification of this important parameter.[36,40]

We started the assessment of this electrochemical utilization by performing cyclic voltammetry measurements on the electrochemically conditioned Pt/C and Pd/C working electrodes used hereafter both in the online GC cell and in RDE, using the catalyst loadings implemented in the former configuration (i.e., 25 vs. 100 $\mu g_{metal} \cdot cm^{-2}$ for Pt/C vs. Pd/C, respectively). The area-normalized CVs recorded on Pt/C in N_2-saturated 0.5 M K_2HPO_4/KH_2PO_4-buffer and Pd/C in CO_2-saturated 0.5 M $KHCO_3$ are displayed in Figs. 6a and Fig. 6b, respectively. The excellent agreement between those CVs confirms that the utilization of these electrodes with the same catalyst loadings (and corresponding layer thicknesses) is fully comparable for the measurements in the GC cell and RDE configuration.

Complementarily, to determine if the utilization of the thick Pd/C catalyst layer used in the GC cell is comparable to that of a thin-film (for which a full utilization can be expected—*vide supra*), we prepared Pd/C RDEs with loadings of 10 and 100 $\mu g_{Pd} \cdot cm^{-2}$ and assessed their electrochemical surface area using CO-stripping. The resulting CO-stripping sweeps and corresponding baseline CVs are displayed in Fig. 7. Here, the ECSAs inferred using the CO stripping charges (estimated based on a normalization charge of 2·205 $\mu C \cdot cm_{Pd}^{-2}$)[37] amount to 106 vs. 78 $m^2 \cdot g^{-1}$ for the measurements performed with loadings of 10 vs. 100 $\mu g_{Pd} \cdot cm^{-2}$, respectively. Notably, the ECSA value inferred in the thin-film configuration (i.e., using a loading of 10 $\mu g_{Pd} \cdot cm^{-2}$) agrees very well with the 107$m^2 \cdot g^{-1}$ which have previously been reported by Mittermeier et al.[37] for the same commercial catalyst. Based on these values and assuming a full utilization of the thin-film, the estimated utilization of the thick layer (i.e., with a Pd-loading of 100 $\mu g_{Pd} \cdot cm^{-2}$) is ≈74 %. This partial utilization stemming from a thick catalyst layer also entails the presence of mass transport limitations within its thickness that are likely to lead to longer retention times of the reactants as well as of the evolved products within the catalyst layer. While the study of these effects lays beyond the scope of this work,

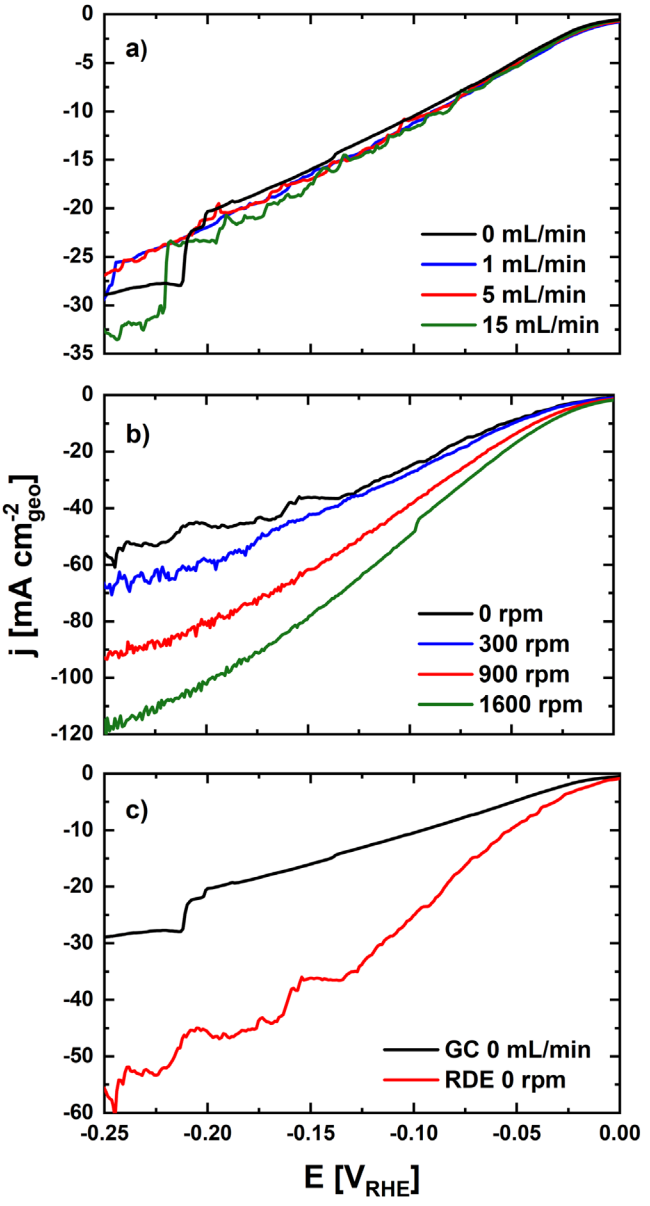

Figure 8. Negative going scans at 10 mV · s^{-1} recorded on 47% Pt/C electrodes (with 25 $\mu g_{Pt} \cdot cm^{-2}$) in N_2-saturated K_2HPO_4/KH_2PO_4-buffer with different gas flow rates in the online gas chromatography (GC) cell (a), or varying rotation rates in rotating disk electrode (RDE) configuration (b). The polarization curves with no induced convection (i.e., RDE with 0 rpm vs. GC cell with 0 mL·min^{-1} of gas flow rate) are also presented in direct comparison in (c).

they can in terms cause higher conversions of the reactants as well as further reduction of the products, thus influencing the measured selectivity of these catalysts.[12]

In the subsequent step, we investigated the convective properties of the online GC cell by performing H_2-evolution measurements on the Pt/C catalyst (in N_2-saturated, 0.5 M K_2HPO_4/KH_2PO_4-buffer) by recording linear sweep voltammograms down to −0.25 V_{RHE}. In doing so, we attempted to tune the convection inside the online GC cell by varying the flow rate of the N_2 gas bubbled through catholyte and anolyte, and also performed analogous measurements with the same working electrode loading and electrolyte in an RDE configuration in which convection was varied by adjusting the electrode's rotation rate. The resulting hydrogen evolution polarization curves are displayed in Fig. 8. Interestingly, while the current densities in the online GC cell were found to be largely independent of the gas flow rate (cf. Fig. 8a), the rotation rate had a significant effect on

the current density in RDE (Fig. 8b), whereby a doubling of the maximum current density at −250 mV_{RHE} was observed from the stagnant electrode upon rotating at 1600 rpm (from ≈60 to ≈120 $mA{\cdot}cm^{-2}$, respectively). The lack of gas flow effect on the measured current in the online GC cell implies that the diffusion layer thickness remains unaffected by this variable, and thus changing the gas flow rate should not lead to significant differences in the surface pH or CO_2 concentration during CO_2 electroreduction experiments,[41] rendering measurements carried out at different flow rates comparable. On the other hand, the comparison between the linear sweep voltammograms without added convection in the flow cell and RDE configuration (i.e. without bubbling or rotation, respectively—cf. Fig. 8c) unveils that significantly larger currents can be achieved in the latter case. We tentatively ascribe this behavior to the differences in the electrode geometries intrinsic to the RDE vs. online GC cell configurations. Specifically, in RDE the electrode is embedded in a PTFE body planar with regards to the disc, whereas the GC cell electrode is held by a protruding body implying the presence of edges where bubbles can accumulate, thus potentially shielding parts of the electrode as gas is evolved. The detachment of these bubbles possibly explains the sudden increases of the current density observed at large overpotentials during the negative scans in the GC cell (Fig. 8a).

H_2-evolution on Pt/C and faradaic efficiency quantification.— The product selectivity of an electrocatalyst for a given (CO_2-reduction) product (e.g., CO) is defined as the fraction of the overall charge at a given potential (Q_{total}) that is devoted to yield that species, or so-called Faradaic efficiency ($FE_{product}$, expressed as a percentage), according to the equation:

$$FE_{product} = \frac{Q_{product}}{Q_{total}} \cdot 100 \quad [1]$$

where $Q_{product}$ corresponds to the product-specific charge. For the gaseous species detected by GC (e.g., H_2, CO), their corresponding number of moles ($n_{product}$) can in terms be quantified based on their mole fraction in the gas chromatogram ($x_{product}$, in ppm_{mol}), the volume of gas injected into the GC loop ($V_{injected}$, in our case 1 ml) and the molar volume of a gas at room temperature and ambient pressure $V_{m,25°C,\,1bar}$ [$24.47{\cdot}10^3$ ml $\cdot mol^{-1}$]:

$$n_{Product,GC} = \frac{x_{product} \cdot V_{injected}}{V_{m,25°C,1bar}} \quad [2]$$

whereas for species dissolved in the liquid phase (like the formate considered in this study), a corresponding number of moles ($n_{Product,liq}$) can be calculated based on the $x_{product}$ value derived from the analytic technique using the equation:

$$n_{Product,liq} = x_{product} \cdot V_{electrolyte} \cdot f_{dilution} \quad [3]$$

where $V_{electrolyte}$ is the volume of electrolyte in the cells' catholyte chamber and $f_{dilution}$ refers to the dilution factor applicable in those cases in which this electrolyte was diluted prior to injection/sampling for analysis (e.g., for our formate quantification IC measurements, $f_{dilution} = 20$, see the Experimental section). Thereafter, $n_{Product}$ is converted into the charge required to produce the corresponding amount of product ($Q_{product}$, in C) using Faraday's law:

$$Q_{product} = n_{product} \cdot z_{e^-} \cdot F \quad [4]$$

where z_{e^-} represents the number of electrons per mol of product exchanged during the reaction and F is the Faraday constant (96485 $C{\cdot}mol^{-1}$). Finally, the total charge (Q_{total} in Eq. 1) within a given duration of the potential hold (t_{hold}) can be subsequently calculated based on the current recorded during that period (I) using the equation:

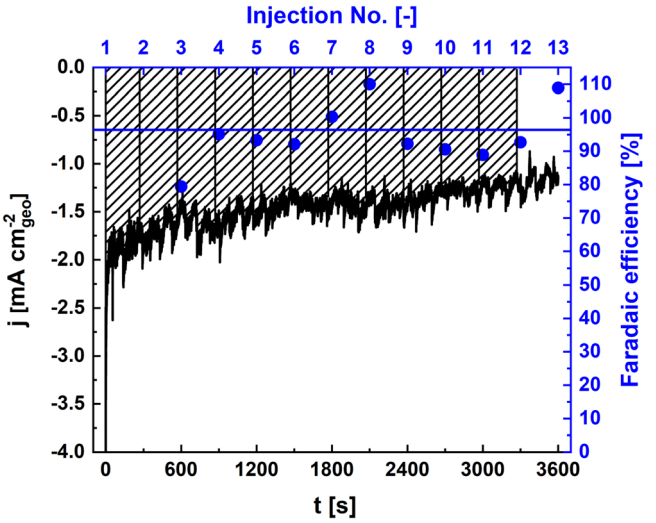

Figure 9. Time evolution of the current in the course of a one-hour potential hold at—25 mV_{RHE} for the 47% Pt/C catalyst in N_2–saturated, 0.5 M K_2HPO_4/KH_2PO_4-buffer (black line) and time-resolved Faradaic efficiency (FE) for each gas chromatograph injection (blue dots). The blue line refers to the average FE value estimated based on injections #4 through #13. The shaded areas illustrate the integration boundaries used to estimate the total charge ($Q_{total,sampling\text{-}res}$) used in the FE calculation (see Eqs. 6 and 7).

$$Q_{total} = \int_{t_0+t_{hold}}^{t_0} I \cdot dt \quad [5]$$

The above approach is excellently suited to the study of CO_2RR-products for which the corresponding $FE_{product}$ values are only estimated at the end of a potential hold (e.g., as in the end-of-test, formate quantification IC measurements included in this work). Using this approach, $FE_{product}$ is determined with the assumption of being constant throughout the potential hold and thereby deliberately ignoring any trends in selectivity over time. However, the use of online analytic techniques (like the GC used here for gaseous products) allows inferring time-resolved selectivities in the course of the electrochemical process, if requiring a more convoluted procedure to estimate the corresponding, time-resolved Faradaic efficiency values ($FE_{product,t\text{-}res}$).

To illustrate this approach, Fig. 9 displays the evolution of the current normalized by geometrical area (j) over the course of a one-hour potentiostatic hold on a Pt/C catalyst at—0.25 V_{RHE} in N_2-saturated K_2HPO_4/KH_2PO_4-buffer—a set of experimental conditions in which H_2 is the only expected reaction product. In that measurement, the first injection of the GC was started with the chronoamperometric hold (i.e., at $t = t_0 = 0\,s$), and 12 additional injections were carried out over the one-hour potential hold.

In principle, $n_{product}$ values can be estimated (using Eq. 2) for the gaseous species evolved in-between each of these product injections, yielding corresponding $n_{product,t\text{-}res}$ and $Q_{product,t\text{-}res}$ values (cf. Eq. 4) every five minutes. Notably, we found that the first injection (at t_0) showed no product, while the second and third injections (at $t = 5$ and 10 min, respectively) usually featured low product concentrations due to the delay required for their equilibration within the catholyte's headspace and tubing. In this regard, one must consider that the tubing and mixing chamber in our system have a combined volume of 55 ml, implying that (at the gas flow rate of 10 ml min^{-1} used in these online GC measurements), a gaseous molecule produced in the electrochemical cell needs a mean time of 330 s to reach the sample loop of the GC. We note in passing that this estimated travel time does not take into consideration the differences among the diffusivities of the evolved gaseous species (e.g., CO vs. H_2), which are likely to lead to molecule-specific (if hard to quantify) discrepancies in his value. Beyond these considerations,

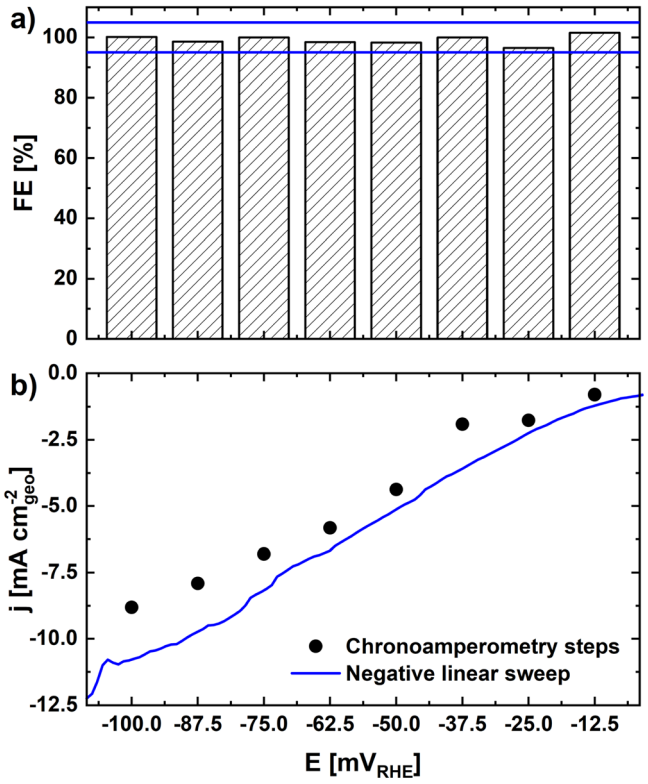

Figure 10. Faradaic efficiencies (FEs) for the evolution of H_2 on 47% Pt/C (25 $\mu g_{Pt} \cdot cm^{-2}$) in N_2-saturated K_2HPO_4/KH_2PO_4-buffer (pH = 6.8) upon measurements at constant potential (a), and the corresponding H_2-evolution polarization curves based on the averaged currents and potentials in these potentiostatic steps vs. a negative linear sweep at a rate of 10 $mV \cdot s^{-1}$ (as presented in figure).

this cell-to-detector delay has implications in the quantification of the time-resolved values of Q_{total} (based on Eq. 5) in the course of these online measurements ($Q_{total,t\text{-res}}$). Specifically for the fourth injection (at t = 900 s), the upper boundary of the integration window for the quantification of this $Q_{total,t\text{-res}}$ corresponds to a time signature $t_0 + t_{hold}$ = 900–330 = 570 s. Concomitantly, the lower integration boundary corresponds to a time signature 300 s (i.e., t_{hold}) earlier in the hold, so that t_0 = 270 s. For all subsequent injections (i.e., #5 to #13 in Fig. 9), the integration windows are consistent with the 5 min spanning in between injections (i.e., t_{hold} = 300 s). An exemption is the third injection, for which the integration boundaries would have only spanned between 0 and 270 s, but for which (as discussed above) we systematically observed a lower-than-expected product concentration.

On top of this, one must keep in mind that only a fraction of the gaseous species produced in the course of these potential holds is injected inside the GC for analysis. More precisely, the time related to this injection ($t_{injection}$) is determined by the volume of the injection loop ($V_{injected}$—in our case, 1 ml, *vide supra*) and the flow rate of the gaseous stream ($\dot{V}_{gas}$) corresponding to 10 $ml \cdot min^{-1}$ for our measurements. Consequently, the charge in between each injection that would have been calculated using Eq. 5 must be weighed for this injection time, as to yield the charge corresponding to the volume of gas injected for analysis ($Q_{total,t\text{-res}}$) using the equation:

$$Q_{total,t-res} = \frac{t_{injection}}{t_{hold}} \int_{t_0+t_{hold}}^{t_0} I \cdot dt = \frac{V_{injected}}{\dot{V}_{gas} \cdot t_{hold}} \int_{t_0+t_{hold}}^{t_0} i \cdot dt \qquad [6]$$

Finally, these time-resolved, product-specific and total charges can be combined to estimate the corresponding time-resolved Faradaic efficiency values in the course of the electrochemical measurement ($FE_{product,t\text{-res}}$), using a modified version of Eq. 1:

$$FE_{product,t-res} = \frac{Q_{product,t-res}}{Q_{total,t-res}} \cdot 100 \qquad [7]$$

The $FE_{product,t\text{-res}}$ values obtained for the employed Pt/C electrode are displayed in Fig. 9. As discussed above, injections #1 and #2 are not shown there, since they took place before the evolved products reach the injection loop (i.e., at t = 330 s, *vide supra*), while for injection #3 a 270 s injection window was used (as opposed to the 300 s of all subsequent injections). As the fourth injection (corresponding to t = 15 min) was found to be the first one corresponding to a stabilized current consistent with the subsequent FE values, the FEs in this and the remaining nine injections were averaged to calculate the final FE_{H2} value of 96 ± 7% derivable from these measurements. Most importantly, this result is consistent with H_2 being the only expected evolved gas under these experimental conditions and validates the FE quantification procedures discussed above and applied in the remaining of this study.

Following the above-described procedures for the estimation of the Faradaic efficiency, we performed additional potentiostatic measurements in a range of −12.5 to −100 mV_{RHE}. The FE values derived from these measurements are displayed in Fig. 10a, while the corresponding polarization curve (potentials vs. averaged currents in these potentiostatic measurements) is compared to one recorded in a negative linear sweep at 10 $mV \cdot s^{-1}$ in Fig. 10b. Notably, all potential-dependent, hydrogen production Faradaic efficiencies are well inside the range of 95 to 105% (see a), thus confirming that the online GC setup and data evaluation approach presented above are accurate in quantifying the gaseous species produced in the cell. On the other hand, the average currents derived from these potentiostatic holds are found to be lower than those in the linear sweep, especially for the larger currents recorded at higher overpotentials. This difference may appear unsurprising when considering the transient nature of the linear sweep; however, we hypothesize that the extended length of the potentiostatic holds (1 h) can be responsible for a part of these deviations, since it may allow for progressive catalyst deactivation (consistent with Fig. 9, and possibly caused by the adsorption of CO and/or impurities in the electrolyte), and/or lead to a partial delamination of the catalyst layer that would be more relevant at larger currents implying the evolution of H_2 bubbles.

CO_2 electroreduction on Pd/C.—Following this important verification, we display the capabilities of the online GC setup for the quantification of the product distribution of a multi-product catalyst requiring detection in both the gaseous and the liquid phase. For this, we used a Pd-based catalyst (20% Pd/C) for which the expected products are H_2, CO, and formate.[4,9,13,20,21] Specifically, at potentials below −0.5 V_{RHE}, CO is reported to constitute the main reduction product, while at higher potentials between −0.4 and 0 V_{RHE}, formate is predominantly produced.

The average Faradaic efficiencies in the course of one-hour potential holds estimated for this 20% Pd/C catalyst are displayed in Fig. 11 and match the selectivity trends reported in the literature discussed above. More precisely, while nearly 100 % of the current is used to produce formate at low overpotentials ($\geqslant$−0.3 V_{RHE}), this $FE_{formate}$ value decreases with increasing overpotential and approaches ≈0% at potentials $\leqslant$−0.7 V_{RHE}. This is accompanied by a shift towards CO production, which is first detected at −0.5 V_{RHE} and subsequently reaches a maximum Faradaic efficiency of ≈70% at −0.7 to −0.8 V_{RHE}, with H_2 production becoming increasingly favorable at even higher overpotentials. Most importantly, these total Faradaic efficiencies add up again to values ranging between 92 and 105 %, with 100% FE included in the error bars at all potentials indicative of the standard deviation among three independent measurements.

Additionally, applying the procedures presented above for the quantification of time-resolved FE values (see Eq. 7), the catalyst's

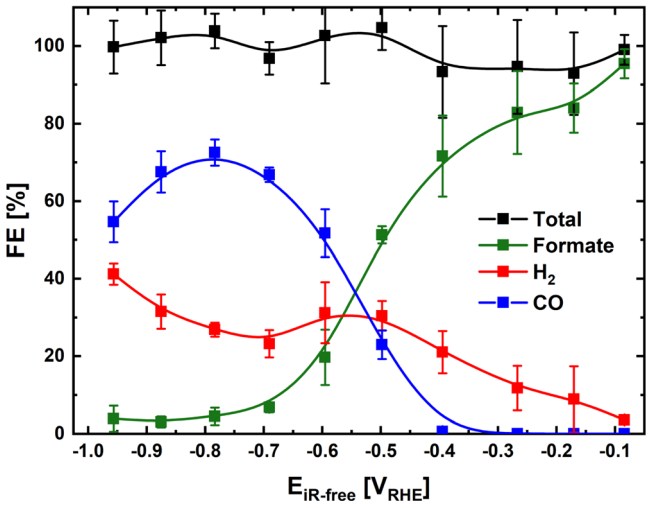

Figure 11. Product-specific selectivities and total Faradaic efficiencies upon CO_2 electroreduction on a 20% Pd/C catalyst in CO_2-saturated 0.5 M $KHCO_3$ averaged over one hour holds at the specified, iR-corrected potentials. Note that each FE value is the average of three independent measurements, with error bars representing their corresponding standard deviations.

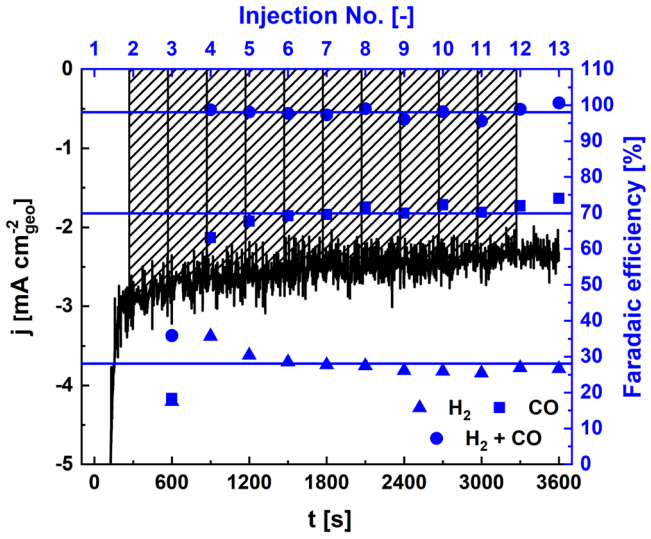

Figure 12. Time evolution of the current throughout a one-hour potential hold at −800 mV_{RHE} for the 20% Pd/C catalyst in CO_2–saturated, 0.5 M $KHCO_3$ (in black), and corresponding, time-resolved Faradaic efficiency (FE) values for H_2 (triangles), CO (squares) production and the sum of both species (circles), respectively. The FE values for the GC injections #4 to #13 are displayed with the blue lines referring to the average FE values based on these injections. The shaded areas represent the integration boundaries used to estimate the time-resolved total charges ($Q_{total,t\text{-}res}$) used in the FE calculation (see Eqs. 6 and 7).

selectivity towards the production of the two gaseous products can be tracked over time. The resulting $FE_{product,t\text{-}res}$ values at a potential of −800 mV_{RHE} are displayed in Fig. 12, which shows how the FE_{CO} increases at the beginning of the potential hold, while the FE_{H2} is decreasing in the same period. This observation can be explained by the formation of a partial layer of CO on the catalyst active surface, shifting the selectivity from H_2 at the beginning towards CO until a dynamic equilibrium is reached.[25] Thereafter, both FEs become stable over the remainder of the one-hour potential hold.

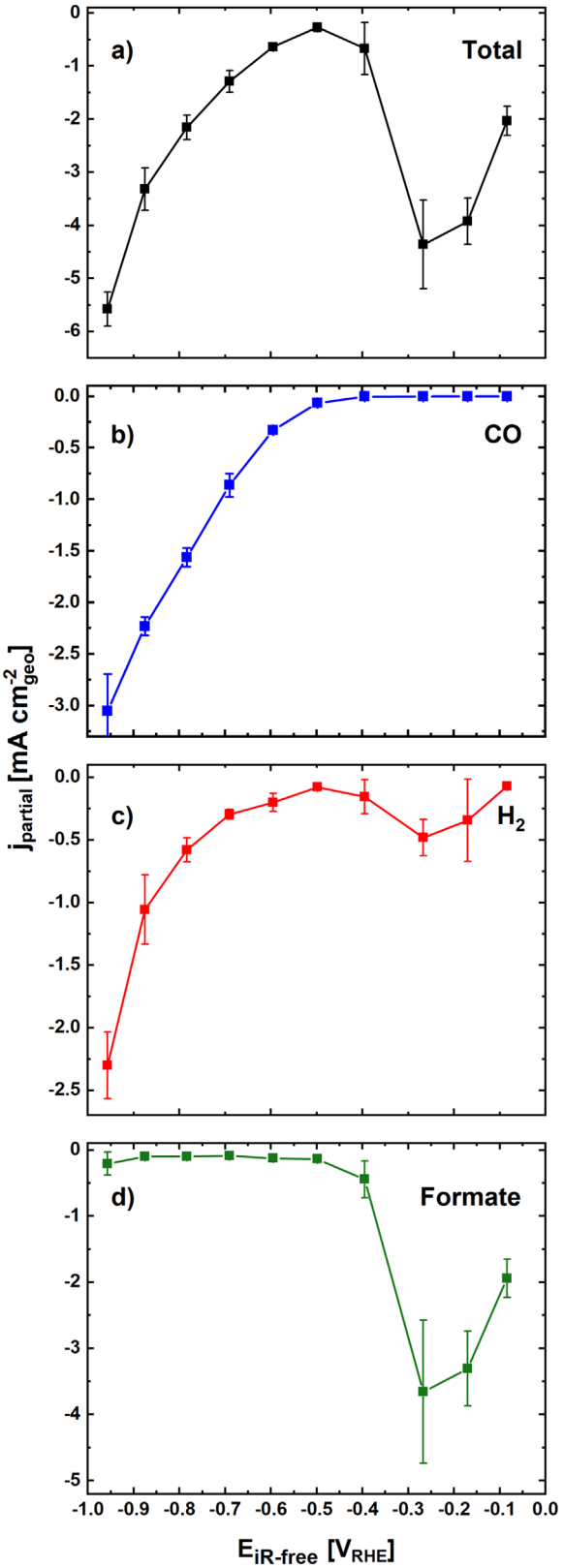

Figure 13. Total current density across the iR-corrected potential range (a) and corresponding, product-specific current densities for H_2 (b), CO (c) and formate (d) production upon CO_2-electroreduction on a 20% Pd/C catalyst (with 100 $\mu g_{Pd} \cdot cm^{-2}$) in CO_2-saturated, 0.5 M $KHCO_3$ are shown as well. All values were averaged from three individual measurements, and the error bars represent the corresponding standard deviations.

This ability to evaluate the time-resolved FEs for different reduction products evolved on a material has the potential to provide valuable insights on reactivity mechanisms and/or catalyst degradation, for example due to changes in the nanoparticles' surface morphology and /or particle size in stability tests.[12,20]

Complementarily, the averaged FE values displayed in Fig. 11 can be used to estimate partial, product-specific current densities by multiplying the average current density at each potential (plotted in Fig. 13a) by the corresponding Faradaic efficiency for each product. The resulting plots are displayed in Figs. 13b-13d, and unveil that, at the higher potentials ($\geqslant -0.3$ V_{RHE}), the partial current densities for both H_2 and formate production increase with increasing overpotential. Thereafter, these currents drop to ≈ 0 $mA{\cdot}cm^{-2}$, and the current density for CO production starts to slowly increase. Notably, while the current densities of formate production stay constant at a negligible level as the potential keeps on decreasing, H_2 production increases again at ≈ -0.6 V_{RHE}, and reaches a comparable value to the one for CO at the lowest tested potential (-2.3 vs. -3 $mA{\cdot}cm^{-2}$ for H_2 vs. CO production at -1 V_{RHE}).

Conclusions

A newly designed, versatile electrochemical cell setup for online gas chromatography measurements applicable for the detection of multiple gaseous as well as liquid products obtained from CO_2 electroreduction was presented. Therein, several improvements in electrode preparation, cell assembly, electrode alignment and contact, and electrolyte to geometrical surface area ratio were proposed. Furthermore, detailed descriptions of the measurement and Faradaic efficiency quantification procedures were provided, along with the importance of electrolyte presaturation.

The electrochemical results obtained in the presented online GC cell were qualitatively compared to those obtained using a rotating disk electrode setup in terms of the mass transport limitations and catalyst layer utilization using a Pt/C catalyst. The same material was subsequently used to validate the cell for gas chromatography product quantification, by verifying that hydrogen evolution accounted for Faradaic efficiencies of $\approx$100% across a range of tested potentials.

Finally, we successfully used the setup to test a commercial Pd/C catalyst for both gaseous and liquid CO_2 electroreduction products (i.e. H_2, CO, formate) by combining online gas chromatography with ion chromatography. Therein, all selectivity trends reported in literature could be reproduced and an assessment of the product-specific current densities as well as of the time-resolved Faradaic efficiencies for gaseous components could be conducted.

Acknowledgments

The authors thank the Swiss Competence Center for Energy Research (SCCER) Heat & Electricity Storage and the Swiss National Science Foundation (SNSF) for funding this project through grant 200020L_178737. J.S.D. thanks Nataša Diklic for her contributions to the data analysis method, Markus Probst for his support with the production of the individual cell parts and is grateful to Thomas Gloor for his support with ion chromatography measurements and the setup of the mass flow software.

ORCID

Justus S. Diercks https://orcid.org/0000-0003-2087-6061
Bernhard Pribyl-Kranewitter https://orcid.org/0000-0001-8777-0996
Juan Herranz https://orcid.org/0000-0002-5805-6192
Thomas J. Schmidt https://orcid.org/0000-0002-1636-367X

References

1. J. Durst, A. Rudnev, A. Dutta, Y. Fu, J. Herranz, V. Kaliginedi, A. Kuzume, A. A. Permyakova, Y. Paratcha, and P. Broekmann, *CHIMIA International Journal for Chemistry*, **69**, 769 (2015).
2. J. M. Spurgeon and B. Kumar, *Energy Environ. Sci.*, **11**, 1536 (2018).
3. J. H. Lee, S. Kattel, Z. Jiang, Z. Xie, S. Yao, B. M. Tackett, W. Xu, N. S. Marinkovic, and J. G. Chen, *Nat. Commun.*, **10**, 3724 (2019).
4. R. Kortlever, I. Peters, S. Koper, and M. T. M. Koper, *ACS Catal.*, **5**, 3916 (2015).
5. M. Valenti et al., *ACS Catal.*, **9**, 3527 (2019).
6. S. Zhu, X. Qin, Q. Wang, T. Li, R. Tao, M. Gu, and M. Shao, *J. Mater. Chem. A*, **7**, 16954 (2019).
7. W. Luc, C. Collins, S. Wang, H. Xin, K. He, Y. Kang, and F. Jiao, *J. Am. Chem. Soc.*, **139**, 1885 (2017).
8. J. J. L. Humphrey, D. Plana, V. Celorrio, S. Sadasivan, R. P. Tooze, P. Rodríguez, and D. J. Fermín, *ChemCatChem*, **8**, 952 (2016).
9. W. Zhu, S. Kattel, F. Jiao, and J. G. Chen, *Adv. Energy Mater.*, **9**, 1802840 (2019).
10. P. Grosse, D. Gao, F. Scholten, I. Sinev, H. Mistry, and B. Roldan Cuenya, *Angewandte Chemie International Edition*, **57**, 6192 (2018).
11. Z. Yin et al., *Nano Lett.*, **19**, 8658 (2019).
12. A. Dutta, M. Rahaman, N. C. Luedi, M. Mohos, and P. Broekmann, *ACS Catal.*, **6**, 3804 (2016).
13. Y. Hori, H. Wakebe, T. Tsukamoto, and O. Koga, *Electrochim. Acta*, **39**, 1833 (1994).
14. K. J. P. Schouten, Z. Qin, E. P. Gallent, and M. T. M. Koper, *J. Am. Chem. Soc.*, **134**, 9864 (2012).
15. F. S. Roberts, K. P. Kuhl, and A. Nilsson, *Angew. Chem. Int. Ed.*, **54**, 5179 (2015).
16. T. Binninger, B. Pribyl, A. Pătru, P. Ruettimann, S. Bjelić, and T. J. Schmidt, *J. Mass Spectrom.*, **53**, 1214 (2018).
17. A. Pătru, T. Binninger, B. Pribyl, and T. J. Schmidt, *J. Electrochem. Soc.*, **166**, F34 (2019).
18. K. P. Kuhl, E. R. Cave, D. N. Abram, and T. F. Jaramillo, *Energy Environmental Science*, **5**, 7050 (2012).
19. W. Ju, A. Bagger, G. P. Hao, A. S. Varela, I. Sinev, V. Bon, B. Roldan Cuenya, S. Kaskel, J. Rossmeisl, and P. Strasser, *Nat. Commun.*, **8**, 944 (2017).
20. M. Rahaman, A. Dutta, and P. Broekmann, *Chem. Sus. Chem*, **10**, 1733 (2017).
21. D. Gao et al., *Nano Res.*, **10**, 2181 (2017).
22. A. S. Varela, C. Schlaup, Z. P. Jovanov, P. Malacrida, S. Horch, I. E. L. Stephens, and I. Chorkendorff, *The Journal of Physical Chemistry C*, **117**, 20500 (2013).
23. D. Vasilyev, E. Shirzadi, A. V. Rudnev, P. Broekmann, and P. J. Dyson, *ACS Appl. Energy Mater.*, **1**, 5124 (2018).
24. Y. Chen and M. W. Kanan, *J. Am. Chem. Soc.*, **134**, 1986 (2012).
25. X. Min and M. W. Kanan, *J. Am. Chem. Soc.*, **137**, 4701 (2015).
26. T. Chatterjee, E. Boutin, and M. Robert, *Dalton Trans.*, **49**, 4257 (2020).
27. C. Zhao and J. Wang, *Chem. Eng. J.*, **293**, 161 (2016).
28. D. T. Whipple, E. C. Finke, and P. J. Kenis, *Electrochemical Solid-State Letters*, **13**, B109 (2010).
29. X. Lu, D. Y. C. Leung, H. Wang, M. M. Maroto-Valer, and J. Xuan, *Renewable Energy*, **95**, 277 (2016).
30. J. Herranz, A. Pătru, E. Fabbri, and T. J. Schmidt, *Current Opinion in Electrochemistry*, **23**, 89 (2020).
31. P. Moreno-García, N. Kovács, V. Grozovski, M. D. J. Gálvez-Vázquez, S. Vesztergom, and P. Broekmann, *Anal. Chem.*, **92**, 4301 (2020).
32. A. A. Permyakova, J. Herranz, M. El Kazzi, J. S. Diercks, M. Povia, L. R. Mangani, M. Horisberger, A. Pătru, and T. J. Schmidt, *Chem. Phys. Chem*, **20**, 3120 (2019).
33. K. Iwase et al., *ACS Appl. Mater. Interfaces*, **13**, 15122 (2021).
34. K. Y. Leung and C. C. L. McCrory, *ACS Appl. Energy Mater.*, **2**, 8283 (2019).
35. M. Ma, E. L. Clark, K. T. Therkildsen, S. Dalsgaard, I. Chorkendorff, and B. Seger, *Energy Environ. Sci.*, **13**, 977 (2020).
36. T. J. Schmidt, H. A. Gasteiger, G. Stäb, P. Urban, D. Kolb, and R. Behm, *J. Electrochem. Soc.*, **145**, 2354 (1998).
37. T. Mittermeier, A. Weiß, H. A. Gasteiger, and F. Hasché, *J. Electrochem. Soc.*, **164**, F1081 (2017).
38. M. Povia, J. Herranz, T. Binninger, M. Nachtegaal, A. Diaz, J. Kohlbrecher, D. F. Abbott, B.-J. Kim, and T. J. Schmidt, *ACS Catal.*, **8**, 7000 (2018).
39. M. Povia, D. F. Abbott, J. Herranz, A. Heinritz, D. Lebedev, B.-J. Kim, E. Fabbri, A. Patru, J. Kohlbrecher, and R. Schäublin, *Energy Environ. Sci.*, **12**, 3038 (2019).
40. T. J. Schmidt and H. A. Gasteiger, *Handbook of Fuel Cells—Fundamentals, Technology and Applications.*, ed. W. Vielstich et al. (Wiley, Chichester) (2010).
41. M. R. Singh, Y. Kwon, Y. Lum, J. W. Ager 3rd, and A. T. Bell, *J. Am. Chem. Soc.*, **138**, 13006 (2016).